Gamma-rays and the evolving, compact structures of the 2003/10/28 X17 flare

C. J Schrijver[1], H. S. Hudson[2], R. J. Murphy[3], G. H. Share[4,3], and T.D. Tarbell[1]

[1]*Lockheed Martin Advanced Technology Center, Palo Alto, CA 94304*
[2]*Space Sciences Laboratory, University of California, Berkeley, CA 94720*
[3]*E.O. Hulburt Center for Space Research, Naval Research Lab., Washington, DC 20375.*
[4]*Astronomy Department, University of Maryland, College Park*

schryver@lmsal.com; hhudson@ssl.berkeley.edu; gerald.share@nrl.navy.mil; ronald.murphy@nrl.navy.mil; ttarbell@lmsal.com

ABSTRACT

The X17 flare on 2003/10/28 was observed by high-resolution imaging or spectroscopic instruments on CORONAS, GOES, INTEGRAL, RHESSI, SOHO, and TRACE. These spacecraft observed the temporal evolution of the γ-ray positron-annihilation and nuclear de-excitation line spectra, imaged the hard-X-ray bremsstrahlung and EUV and UV emission, and measured the surface magnetic field and subphotospheric pressure perturbations. In the usual pattern, the onset of the flare is dominated by particle acceleration and interaction, and by the filling of coronal magnetic structures with hot plasma. The associated positron annihilation signatures early in the impulsive phase from 11:06 UT to 11:16 UT have a line-broadening temperature characteristic of a few hundred thousand Kelvin. The most intense precipitation sites within the extended flare ribbons are very compact, with diameters of less than 1,400 km and a 195 Å TRACE intensity that can exceed 7,500× the quiescent active-region value. These regions appear to move at speeds of up to 60 km/s. The associated rapidly-evolving, compact perturbations of the photosphere below these sites excite acoustic pulses that propagate into the solar interior. Less intense precipitation sites persist typically for several minutes behind the advancing flare ribbons. After ~ 1 ksec, the flare enters a second phase, dominated by coronal plasma cooling and downflows, and by annihilation line radiation characteristic of a photospheric environment. We point out 1) that these detailed observations underscore that flare models need to explicitly incorporate the multitude of successively excited ENVIRONMENTS WHOSE EVOLVING SIGNALS DIFFER AT LEAST IN THEIR TEMPORAL OFFSETS AND ENERGY BUDGETS IF NOT ALSO IN THE EXCITING PARTICLE POPULATIONS AND PENETRATION DEPTHS, and 2) that the spectral signatures of the positron annihilation do not fit conventional model assumptions.

Subject headings: Sun: flares — Sun: X-rays, gamma rays — sunspots

1. Introduction

The general concept of a solar flare is that a sudden relaxation of the coronal magnetic field from a stressed state through magnetic reconnection produces large amounts of high-energy particles. The total energy in the ensemble of non-thermal electrons and ions may amount to a large fraction of the total flare energy (e.g. Lin and Hudson 1976; Ramaty *et al.* 1995; Emslie *et al.* 2005). These particles eventually thermalize through interaction with plasma from corona to chromosphere and below, unless they escape into the heliosphere.

The solar atmosphere into which the non-thermal particles precipitate is not simple: flares generally occur in active regions with strong, highly structured magnetic fields, and the flare process itself perturbs the atmosphere, sometimes down to photospheric levels. Moreover, as this study confirms, the dominant particle-acceleration and particle-precipitation sites move over distances that may exceed their typical width within a minute. Such motions are most commonly seen as moving flare ribbons in, e.g., Hα or in (E)UV image sequences by the TRACE spacecraft (e.g., Fletcher *et al.* 2005, who use this to measure reconnection rates by comparing the footpoint motions with magnetograms).

The flare energy sources move, creating a sequence of disjoint atmospheres contained by flux tubes that evolve through excitation and subsequent relaxation with different time delays. Consequently, a low-resolution instrument may see contributions from multiple such evolving atmospheres simultaneously (e.g., Warren and Doschek 2005) while high-resolution imaging instruments may see different signatures evolve with time histories more characteristic of the physical processes that are involved.

In this paper we compare and analyze unique observations of the X-17 flare on 2003/10/28 that were made with six different spacecraft with imaging and/or spectroscopic instruments. These instruments cover the wavelength domain from γ-rays to the visible and provide the most comprehensive high-resolution data set with which to study the evolution of these evolving atmospheres of a major flare.

We use this excellent set of observations to develop a scenario for the flare evolution that includes the impact of high-energy particles on the near-photospheric atmosphere under the flare. In particular, the high-resolution imaging by the TRACE spacecraft and the high-resolution γ-ray spectroscopy by the RHESSI spacecraft lead us to conclude that energy release occurs in compact domains that propagate through the coronal volume, causing a series of plasma atmospheres to evolve one after the other as the flare progresses. Even within

this comprehensive array of data, however, we find no ready explanation for the evolution of the positron-annihilation line width observed by RHESSI (Share et al., 2004).

2. Observations

The initial phase of the X17 flare studied here was imaged by RHESSI, SOHO, and TRACE, and observed by GOES, INTEGRAL, and CORONAS. We describe these observations in this section, summarizing key evolutionary stages in Table 1 and Fig. 1. Movies of the SOHO/MDI magnetogram data and of the TRACE 1600 Å and 195 Å channel images are available in the on-line version of this paper.[1]

2.1. GOES, INTEGRAL, CORONAS

The GOES-12 spacecraft observed the X17 flare on 2003 October 28 in NOAA active region 10486 starting at approximately 9:51 UT, when the signal climbs from mid-B to M1 levels by 10:59 UT, after which it increases rapidly to peak at approximately 11:10 UT in the $1-8$ Å pass band. The GOES light curve, saturated around the flare peak from ∼11:06 to ∼11:16 UT, shows that the flare increased the Sun's soft X-ray radiance by a factor of over ~ 200. Although the NOAA listing formally ends the flare at 11:24 UT, the long, gradual decay continued for over 12 h before the pre-flare emission level was approached.

The INTEGRAL/SPI lightcurves show that the most energetic part of the flare starts around 11:02:30 UT with a minute-long spike, followed by somewhat irregular decay of the intensities with time (Gros *et al.* 2005). CORONAS data show that the first peak is dominated by bremsstrahlung up to 30 MeV and that high-energy γ-rays from pion production begin to be observed around 11:04 UT (Kuznetsov *et al.* 2005). The INTEGRAL anti-coincidence shield (ACS) rates above 100 keV are shown in Fig. 1a, scaled to the RHESSI 200 keV bremsstrahlung intensity.

2.2. RHESSI

The Ramaty High-Energy Solar Spectroscopic Imager, RHESSI (Lin *et al.* 2003), was traversing the high-radiation zone of the south-Atlantic magnetic anomaly for most of the rapid rise phase of the flare, including its peak, until 11:06 UT. Because of the flare's magnitude, the RHESSI front detectors saturated below 20 keV even with the attenuators in place early in its flare observations, so that we have little reliable data on X-rays for those energies.

The RHESSI observations of solar γ-radiation enable analysis of the line and continuum shapes of the γ-ray emission. Most of the γ-ray spectral lines reflect nuclear de-excitation transitions that promptly follow the inelastic scattering of primary ions on target nuclei, but the strong 2.2 MeV line resulting from deuterium formation by neutron capture and the 0.511 MeV positron-annihilation line (and continuum below the line) have different physical origins and provide different diagnostic information (e.g., Ramaty *et al.* 1975). Both of these lines require the slowing-down of secondary nuclear products – neutrons and positrons, respectively – in the solar atmosphere, perhaps as deep as the sub-photospheric layers.

Share *et al.* (2004) study the evolution of the RHESSI γ-ray spectrum after 11:06 UT. They analyze the 0.511 MeV positron annihilation line strength and width and compare that to 200 keV bremsstrahlung, the total nuclear de-excitation line flux in the RHESSI spectra, and the annihilation continuum flux (Fig. 1a, b). Their estimated plasma temperatures and lower limits on the atomic densities are listed in Table 1, using labels a-d as in their paper. The temperatures are derived assuming that the annihilation line width is primarily due to thermal broadening. The plasma densities are lower limits derived under the assumption that the continuum at energies below the 0.511 MeV annihilation line is associated with positronium continuum. Much higher densities would be required if the continuum came from Compton scattering of the 0.511 MeV line photons in the much denser atmosphere if the positrons were to originate from decay of pions as may be inferred from CORONAS observations early in the flare. Share *et al.* conclude that in the initial two minutes after 11:06 UT, the positrons annihilated in an environment at temperatures of approximately 300,000 K but with at least a chromospheric density exceeding 10^{11} cm^{-3}. The line width measurements up until 11:16 UT continue to indicate temperatures above 10^5K and increasingly higher lower limits on the densities. After 11:18 UT the annihilation spectra are consistent with photospheric temperatures and densities ($> 10^{15}$ cm^{-3}).

We note here that even as the RHESSI 200 keV electron bremsstrahlung shows a persistent exponential decrease with a 3.6 min. e-folding time scale (dotted line in Fig. 1a), the total nuclear de-excitation signal transitions around 11:18 UT from that same decay profile to a decay with an e-folding time scale of ~ 20 min. At that time, the 0.511 MeV line narrows markedly (Fig. 1b), after which the total nuclear de-excitation signal decays proportionally to the 0.511 MeV line intensity (Fig. 1a). We note that the 0.511 MeV intensity is well described by a sum of two exponentials, with time scales of 3.6 and 20 min. (solid smooth curve in Fig. 1a, and repeated in Fig. 1c for comparison with the 1600 Å signal discussed in § 2.3).

RHESSI provides γ-ray images of solar flares for the first time (Hurford *et al.* 2003, 2006). Interestingly, in two of four events analyzed, the ion precipitation regions as inferred

from the 2.2 MeV neutron-capture emission appear to differ significantly from the electron precipitation regions as inferred from the bremsstrahlung continuum; in the other cases the differences are not significant. In the X17 flare studied here, the 2.2 MeV regions are clearly resolved into a double-footpoint structure with centroids about 15″ east of the corresponding hard X-ray bremsstrahlung centroids (see the circles in Fig. 2d for approximate positions). Hurford *et al.* (2006) point out that this difference persists even when a $\sim$ 100 s delay is allowed for to approximate the time needed for the secondary neutrons to thermalize and be captured. We return to this in Sect. 3.

2.3. TRACE

The Transition Region and Coronal Explorer, *TRACE* (Handy *et al.* 1999), observed the X17 flare in interlaced sets of the 1600 Å channel (dominated by the strongest UV emission lines, such as the C IV doublet, and - particularly during flares - the UV continuum) and the 195 Å channel (Fe XII in quiescence, with an often dominant contribution of Fe XXIV or thermal continuum during flares). An occasional broad-band visible ('white light') image was taken for precise co-alignment with SOHO's MDI.

During the interval from 11:00 UT through 11:20 UT studied here, TRACE observed the Sun primarily in the 195 Å channel at a cadence of a few seconds (depending on its exposure time and the details of other interspersed images); a summary movie with frames at approximately 2 min. cadence is shown in the electronic addenda. The automatic exposure control for the 195 Å channel could not follow the rapid evolution of the brightness of the flare, despite the fact that the exposure durations rapidly shortened by a factor of 100 going into the flare peak.

The 1600 Å passband observations were taken with a cadence close to one minute. Most of the 1600 Å exposures were very short ($\approx$ 0.1 s) and showed only the brightest features on a noisy background. Longer exposures (0.8 s) in the 1600 Å channel, which show both flare and non-flare features, were taken at intervals of approximately 6 min.; a movie of these longer exposures is shown in the electronic addenda to this paper.

Neither the 195 Å images nor the 1600 Å images properly cover the full dynamic range of the flare intensity. Most images thus show many saturated pixels. For very compact saturated sources, the diffraction pattern formed by the support grid of the front filter for the 195 Å channel can be used to estimate the intensity of the zeroth order by looking at higher-order intensities. There is no such diffraction pattern for the 1600 Å image, but the signal in some of the bright kernels is so strong that it caused CCD blooming in the relatively

long context images, which was the first time this was ever noticed in TRACE images. These effects are discussed in Secs. 2.3.1 and 2.3.2, respectively.

The total TRACE 1600 Å channel signal in the flare (corrected for the pre-flare level) is shown in Fig. 1c. Its overall behavior after peaking at $\sim 11:04$ UT is similar to that of the total nuclear de-excitation signal, first decaying on a 3.6 min. time scale (dotted line), then transitioning to a 20 min. e-folding time scale (dashed line) that persists for at least one hour past the flare peak. In this later phase, the 1600 Å channel scales with time as the GOES $0.5-4$ Å X-ray signal. The total 1600 Å signal is well approximated by a double exponential ($1.2\times10^4\exp(-t/3.6)+750\exp(-t/20)$ DN/s), shown by the thin solid curve in Fig. 1c; this double exponential, with a different scaling, was shown to approximate the RHESSI 0.511 MeV intensity in Fig. 1a. The best approximation of the 1600 Å channel is given by the set of shortest exposures (largest symbols), because these suffer least from detector saturation which causes artificially low average intensities (as seen from the smaller, lower-lying symbols used for the longer exposures).

The TRACE 195 Å flare signal suffers from strong saturation prior to approximately 11:14 UT, and some even after this. The signal from 11:14 UT onward evolves similar to the GOES $0.5-4$ Å X-ray signal (Fig. 1d), decreasing roughly as $85\exp(-t/20)$ DN/s (dashed line through the shortest exposures). The cycling through different exposure durations, with different fractions of the CCD at saturated levels, causes the sets of exposures to show up as nearly parallel sequences, with the shortest, least-saturated exposures at the top.

2.3.1. Brightness and size of the dominant particle precipitation sites

The TRACE observations of very bright kernels within the UV and EUV flare ribbons suggest that the energetic particle precipitation is particularly strong in a few compact sites, consistent with the RHESSI bremsstrahlung observations (the strongest bremsstrahlung coincides with sites of pronounced diffraction crosses in the 195 Å signal, see Hurford *et al.* (2006)). For example, the 1600 Å TRACE image at 11:06:21 UT (with an exposure duration of 0.9 s) shows flare ribbons that are saturated at the maximum of the 12-bit analog-to-digital conversion at a data number, or DN, of 4096 over much of their area. Within these areas, some compact regions stand out particularly, because they are so bright that they cause CCD blooming, reflected in extended, horizontal stripes in the image. Two such sources are seen in the lower ribbon, two in the upper ribbon, in only a single exposure (cf., Fig. 2d).

The charges accumulated onto the CCD in these bright points in the 1600 Å image have spread out over the length of the blooming strips of 140 to 180 pixels. Given the nonlinear

CCD response near the saturation electron content of the detector pixels ("full well"), the loss of information in the 12-bit A-D conversion, and the saturation in both the bright points and the surrounding ribbons, we cannot accurately determine the brightness contrast between the kernels and the surrounding ribbons directly. We use the blooming-strip length as a measure for the minimum brightness, which yields at least $4096 \times 180 = 0.7 \times 10^6$ DN/s. Images taken earlier at 11:04:25 UT and 11:05:01 UT, with short exposure times of 0.0032 s and 0.0048 s respectively, are not saturated, and have peak brightnesses of $(0.6 - 1.0) \times 10^6$ DN/s, comparable to the estimate based on the blooming artifacts. The minimum contrast with the surrounding non-blooming, saturated ribbons is at least a factor of ~ 150, and with the surrounding quiescent plage at least a factor of $4,000$.

The blooming features allow us to determine the central location of the bright points within the flare ribbons rather accurately (see Fig. 2d). In contrast, the intensity history of these brightest features is not well constrained by the TRACE observations. Exposures taken before 11:04 UT are saturated from an exposure at 11:01:06 UT onward. The latter exposure shows no bright features yet near the location of the CCD blooming. As already pointed out, the exposures taken at 11:04:25 UT, 11:05:01 UT, and 11:06:21 UT have comparable peak brightnesses. Exposures remain saturated, despite exposure times that are $10\times - 100\times$ shorter than that at 11:06:21 UT, until 11:08:39 UT. After that, the brightest features fade, reaching $\sim 0.1 \times 10^6$ DN/s in the exposure at 11:09:51 UT, and continuing to fade after that.

Another very bright kernel in the flare ribbons, seen in the 195 Å image at 11:07:41 UT (green dot in Fig. 2d), is saturated so that we can place only a direct lower limit on its brightness of $\sim 4,000$ DN/s. One feature of the TRACE 195 Å channel is that the front-filter support grid causes a diffraction pattern. The brightest features are thereby seen repeated in the cross formed by the diffraction orders. This diffraction pattern can be used to evaluate the intensity (and size, see next section) of the saturated kernel. Using the intensities in the first few orders of the diffraction pattern (Lin *et al.* 2001), we estimate that the peak intensity level in the kernel reached approximately $20,000$ DN/s, or $7,500\times$ brighter than the typical quiescent plage, and more than an order of magnitude brighter than the surrounding flare ribbons. If the Fe XII line at 195 Å dominates that emission, a density contrast of at least a factor of 90 is required compared to the quiescent plage, but we realize that Fe XXIV or high-temperature (or non-thermal) continuum emission are likely to contribute substantially; these may require even higher densities.

2.3.2. Apparent size and motion of the most prominent precipitation sites

The 195 Å diffraction patterns show the full width at half maximum of the brightest features to be ~ 4.2 TRACE pixels of 0.5 arcsec or 375 km in size. Taking into account the TRACE resolution of ~ 750 km, we conclude that they extend over no more than 1,400 km.

The brightest features in, for example, the TRACE 1600 Å channel are saturated and surrounded by other bright features so that we cannot use that information to estimate the width of the most prominent precipitation sites as we do for the 195 Å channel. The data can be used, however, to track the displacement history of these features from 11:06:21 UT, when they cause CCD blooming, to 11:11 UT when they reach the compact polarity artifact in the MDI magnetogram at P_2 (Fig. 2a) which is discussed in Sect. 2.4.1. In this time interval, the precipitation footprint has moved over approximately 16,000 km. With the corresponding average migration speed of ~ 60 km/s, we conclude that a high-energy particle "beam" with a width of $< 1,400$ km travels over its own width in $\tau_{\rm w} < 23$ s at least up to approximately 11:12 UT. The saturation of the 1600 Å images makes it harder to estimate a propagation velocity for the conjugate site moving into the eastern, negative spot at P_3, but the magnetogram artifacts, discussed in § 2.4 stand out quite clearly. They advance rapidly westward until approximately 11:14 UT, with an estimated propagation speed of ~ 30 km/s.

According to the standard reconnection scenarios, the apparent motion of the footpoints reflects the rate of reconnection in the corona. We would like to compare this with the Alfvén speed v_A in the corona, but we do not have a good magnetic model for the structure. Taking nominal values of $B > 100$ G and $n_e = 10^9\,\mathrm{cm}^{-3}$, the observed footpoint motion would correspond to coronal reconnection progressing at $< 0.05\mathrm{v}_A$.

2.4. SOHO/MDI

2.4.1. Magnetic signal

SOHO/MDI observed the event in a full-disk, high-cadence mode, measuring both the velocity signal (discussed in the next section) and the magnetogram signal at 1-min. cadence. The magnetograms show the gradual evolution of the complex magnetic field, which shows a ridge of opposite polarity features included within a penumbra in common with the main, trailing, positive-polarity spot (see Figs. 2a and b).

Starting at 11:02:30 UT, however, rapidly evolving image artifacts show up in the strong field environments, under the flare ribbons seen with TRACE. The strongest such artifacts appear as pronounced polarity inversions (marked $P_{1,2,3}$). This occurs first in the positive-

polarity spot near P_1 (in Fig. 2a) around 11:04:30 UT, which rapidly fades away. They strengthen again around 11:11:30 UT, now occurring in a compact region in the western side of the positive-polarity umbra near P_2. There, the apparent polarity returns to the proper positive value around 11:15:30 UT. This magnetogram artifact continues to fade, and is no longer visible from about 11:21:30 UT. Similar moving, evolving magnetogram artifacts show up in the western, negative umbra around P_3 after 11:06:30 UT, seen until about 11:19:30 UT. Note that whereas the fronts of these artifacts advance quite quickly until about 11:11 UT, most artifact locations persist over ∼5 min. or more before fading. Apparently the perturbation crossing time scales estimated in § 2.3.2 for the most pronounced precipitation kernels is short compared to the duration of particle precipitation onto much of the rest of the flare ribbons.

These artifacts are likely a consequence of a strong distortion of the Ni I 8768 Å magnetic diagnostic line. As discussed by Qiu and Gary (2003), magnetogram artifacts suggest that the line turns into an emission line, or that it at least shows a strong central reversal in the regions most strongly affected by the particle populations that cause the flare ribbons. Ding *et al.* (2002) show that an emission profile is readily formed as an electron beam impacts on the supra-photospheric layers up to the chromosphere, particularly if that happens in a relatively cool atmosphere like that of a spot umbra. In their scenario it is the nonthermal collisional excitation and ionization of the hydrogen atoms that shifts the line and nearby continuum formation heights upward, and that can cause the line to become an emission line. It may also be possible to form an emission line by forming a temperature-minimum zone, likely resulting in the formation of an inversion layer, i.e., a dense chromosphere for neutral nickel, with temperatures high enough to populate the first excited level, but well below the characteristic temperature of order 90,000 K associated with its ionization energy of 7.63 eV. Ding *et al.* (2002) show, however, that standard atmospheric stratifications for active and flare atmospheres like the VAL3C (Vernazza *et al.* 1981) and F1 (Machado *et al.* 1980) models result in simple absorption line profiles.

As one measure for the footprint of the particle precipitation sites we show the evolution of the total area of the magnetogram artifacts (traced by time-tagged pixels in Fig. 2a) in Fig. 1e. For this purpose, we identify pixels as magnetogram artifacts if their signal changes by 50 Mx/cm^2 or more from one magnetogram to the next. It is interesting to note that the total area of the magnetogram artefacts scales as the intensities observed for the INTEGRAL/SPI and RHESSI nuclear de-excitation lines (also shown in Fig. 1e).

2.4.2. Acoustic signal

The SOHO/MDI velocity data are analyzed by Donea and Lindsey (2004), who find that the X17 flare excites sunquakes, coupling into the solar interior primarily in two places. They find a source with a peak intensity around 11:04 UT near the location labeled P_1 in Fig. 2a, with a FWHM uncertainty in that peak time of 8 min. The second source peaks around 11:07 UT, and is located near P_3 (in Fig. 2a) in the umbra of the negative, western spot. Both of these acoustic sources appear to be associated with strong energy deposition sites. RHESSI detected a hard X-ray source at P_3 after 11:06 UT (Hurford *et al.*, 2006) and TRACE 1600 Å and 195 Å images of the flare ribbons provide indirect evidence of energy deposition at both sites.

3. Ion collisions, positron annihilation, and the 0.511 MeV line

To set the stage for the integrating discussion of the flare observations in the next section, we here briefly outline relevant aspects of particle interactions, radioactive decay, and possible sources of broadening for the 0.511 MeV annihilation line.

Interaction column depths exceeding $0.02\,\mathrm{g/cm^2}$ and $0.3\,\mathrm{g/cm^2}$ are typically required to produce 80% of the β^+-unstable nuclei and positive pions, respectively, in flares (Murphy *et al.*, 2006). In the classical interpretation of direct impact, such column depths are reached deep in the chromosphere or in the photosphere (below at most $h = 600\,\mathrm{km}$ in VAL models P, for characteristic plage, and F, for a flaring atmosphere; cf. Vernazza *et al.* (1981)). The positrons emitted in these decays typically have energies of $\sim$0.5 MeV and 30 MeV, with corresponding characteristic ranges prior to annihilation of $\sim 0.08\,\mathrm{g/cm^2}$ to $6\,\mathrm{g/cm^2}$, respectively.

If we assume that the positrons emitted by decaying pions do not escape from the photospheric depths where they are produced, most of the associated 0.511 MeV annihilation-line photons will be Compton scattered out of the 0.511 MeV line to lower energies. Almost all of 0.511 MeV line photons that are detected by RHESSI from the flare will therefore have originated from radioactive decay of β^+-unstable nuclei. Our calculations indicate that only $\sim 50\%$ of the positron emission will have occurred within 5 min of the interaction. This is important given the rapid evolution of the flare and the migration of the particle-acceleration sites as reflected in the ribbon motions.

What are the possible cuases for the large initial width of the 0.511 MeV annnihilation line? Whereas detailed transport calculations have yet to be performed to determine what fraction of the positrons can escape from their deep production region to higher altitudes in the solar atmosphere, we can rule out that they annihilate in loops that are maintained at temperatures of a few hundred thousand Kelvin along their length: the TRACE UV data show well-separated conjugate precipitation regions forming the flare ribbons. Therefore, we rule out the possibility of thermal broadening of the 0.511 MeV line from annihilation in such loops.

Bulk turbulent motion is, in principle, an alternative cause for the large width of the 0.511 MeV annihilation line observed from 11:06 - 11:16 UT. We rule out this option too, however, because of the widths of some of the nuclear de-excitation lines observed by RHESSI. If the medium in which positrons were emitted and annihilated exhibited substantial turbulence, this turbulence should also broaden the nuclear de-excitation lines (scaled proportional to energy). The 0.847 MeV ^{56}Fe and 1.36 MeV ^{24}Mg lines integrated from 11:06:20 UT to 11:10:20 UT have FWHM values of 3.5 ± 2.6 keV and $10. \pm 3.$ keV, respectively. These widths are narrower than those expected for impact by a downward directed particle population. The widths are also narrower at the 2.9σ and 2.3σ uncertainty levels than the values of 11 keV and 17 keV that should have been observed if the 0.511 MeV line had been turbulently broadened in the same environment. Based on these arguments we conclude that the 0.511 MeV line is most likely thermally broadened in relatively compact regions.

4. In conclusion: a scenario with missing pieces

The observations of the X17 flare that we analyze here appear in some respects to be consistent with the standard scenario of energy deposition by non-thermal particles, and with the theory of flare γ-ray emission within the framework of nuclear interactions with simplifying assumptions about the propagation of the primary and secondary particles (e.g., Ramaty *et al.* 1995, and references therein).

In particular, the first 1 ksec of the flare, forming Phase I, appears consistent with the usual picture of particle precipitation (causing the flare ribbons) and chromospheric evaporation leading to the brightening of the coronal loops. After a few early impulsive variations, we see the particle interaction rate decline exponentially on a time scale of $\sim$3.6 min from about 11:05 UT to $\sim$11:16 UT (Fig. 1a). In this phase, the energetic electrons cause a bright but

rapidly decreasing bremsstrahlung continuum as they impact the plasma, which decreases in proportion to the nuclear de-excitation line flux after 11:10 UT. The impact sites of the energetic particles as reflected in the UV flare ribbons propagate rapidly, up to several tens of km/s for the strongest sites, with continuing afterglow lasting for up to several minutes behind the flare-ribbon fronts.

An unusual feature of this strong flare is that it induced observable seismic waves in the solar interior. In their seismic study of MDI Doppler data, Donea and Lindsey (2004) argue that for an atmospheric signal to efficiently couple into the photosphere, the time scale characteristic for the perturbation as determined by the acoustic cutoff frequency and the photospheric pressure scale height is $\lesssim 40\,\mathrm{s}$. Our estimate for the time τ_w (see Sect. 2.3.2) for the most intense precipitation sites to propagate over their own diameter, meets that requirement. It is thus likely that the most impulsive flare processes in the solar corona excite some positions in or near the photosphere so strongly that this couples to detectable helioseismic waves in the solar interior. These perturbations may be caused by the energy deposition of precipitating high-energy particles or by the resulting radiative backwarming, or by a field realignment (the latter was suggested for other flares by Sudol and Harvey (2005)).

The flare differs from the standard scenario in several aspects. For one thing, the apparent offsets between the ion and electron precipitation regions (Hurford *et al.* 2003, 2006, see the circles in Fig. 2d) suggest that these two particle populations do not necessarily impact the same region at the same time. We note that the roughly 100 s needed for the neutrons to thermalize prior to their capture should cause their emission to come from a site where the instantaneous electron bremsstrahlung would have been seen ∼100 s before; for a characteristic propagation velocity of 60 km/s, that offset could reach up to ∼ 8 arcsec. However, Hurford *et al.* (2006) find that a rough correction for such a 100 s delay does not lead to such large position offsets.

Another aspect that is at odds with the standard flare scenario concerns the positron annihilation radiation. In order for the bulk of the positrons to annihilate in the warm medium needed to thermally broaden the annihilation line, the ions need to impact onto, and the positrons need to be emitted into, a plasma at several hundred thousand Kelvin with a total column depth of at least several tenths of $\mathrm{g/cm^2}$ (see Sect. 3), or a column density of $N_\mathrm{H} \gtrsim 10^{22}\,\mathrm{cm^{-2}}$. The required ion impact might be achieved

near the coronal base if multiple mirroring could occur in the coronal field, but it is hard to imagine how the $\sim 10^5$ K plasma thus heated could remain dense and thick enough for several minutes to allow for positron emission and annihilation in it before the plasma streams up into the coronal volume (where it is responsible for the flare's X-ray emission).

Perhaps there is a way to maintain an unexpectedly thick layer at transition-region temperatures for several minutes below the coronal base in a highly dynamic atmosphere. The atmospheric response to particle precipitation and the associated chromospheric evaporation continue to be studied in 1D radiation hydrodynamic models, and some show that a relatively thick transition region with temperatures of order 10^5 K and above can indeed form (e.g., Allred *et al.* 2005, and references therein). It is presently unclear how such a region can be made thick enough, and made to last long enough, to allow the bulk of the positrons to annihilate in a warm environment at least temporarily. Such warm environments need to persist longer than the few-minute radioactive time scale for positron emission of multiple minutes (Sect. 3). Note that this time scale is comparable to, and for the brightest sites exceeds, the time scale for the displacement of the precipitation sites as inferred from footpoint crossing times (here we make the assumption that we can identify the UV and hard X-ray sources and the other compact footpoint signatures as resulting from a common exciter). This suggests at the very least some sustained energy deposition behind the precipitation front.

Alternatively, the broad annihilation line originates in much deeper layers of the solar atmosphere. This requires that the energetic ions penetrate well below the classical chromosphere, as they well may (see Sect. 3), and that enough energy is deposited in these dense layers to raise the temperature to several hundred thousand Kelvin. This energy deposition should more or less balance the strong radiative losses for several minutes after the initial nuclear excitation in order to have enough time for the positrons to be emitted and annihilated in a warm, dense environment. Observational support for this hypothesis is found in the anomalies in the magnetogram series and in the UV flare ribbons around points $P_{2,3}$. These persist at any given location for up to ~ 5 min., and are conceivably associated with a warm, dense medium. Such a large volume of warm plasma could be very luminous if not optically thick, however, because the temperature is at the peak of the plasma emissivity function. Models will need to be developed to assess whether this scenario is tenable.

Regardless of how the $\sim 10^5$ K plasma is heated, the observations require that any model for the early positron annihilation for this flare must approximate the integrated signal from multiple differentially-evolving atmospheres. Apparently, the temporal behavior of energetic particles exciting these atmospheres can be a mix of a strong initial beam that rapidly moves on, followed by some persistent precipitation for up to several minutes after that.

Then, as the magnetogram artefacts disappear, as the flare ribbons slow down, and as the time scales for the falling fluxes of nuclear de-excitation and electron bremsstrahlung no longer match, we see the positron annihilation signatures shift to what appears consistent with a deep chromospheric or photospheric environment: in this Phase II of the event, the narrow 0.511 MeV line appears to originate in an environment with a temperature of no more than $\sim 7,000$ K and an ambient ion density in excess of $10^{15}\,\mathrm{cm}^{-3}$. RHESSI data allow the time-scale for the change in positron line width to be as long as 150 s, but that is an upper limit. As we mentioned in Sect. 3, the nuclear decay time (dependent on the mix of radioactive nuclei and the accelerated-ion spectrum, e.g., Kozlovsky *et al.* (1987); Murphy *et al.* (1987)), may be comparable to that. In contrast, the radiative cooling time is as much as two orders of magnitude shorter than that (Raymond *et al.* 1976).

Our analysis of combined observations by the CORONAS, GOES, INTEGRAL, RHESSI, SOHO, and TRACE satellites shows the power of combining high resolution in the temporal, spectral, and spatial domains. The observations demonstrate that whereas the highly-energetic particle populations precipitate in ribbon-like structures, the emissions are dominated by a few compact precipitation sites which move rapidly through a variety of atmospheric environments as seen in white-light flares observed by TRACE and RHESSI (Hudson *et al.* 2006). Consequently, hard X-ray and γ-ray spectra taken with moderate to low spatial resolution are composite spectra with contributions from a variety of rapidly evolving atmospheres. Combined with high-resolution imaging, the evolution of spectral features, such as the 0.511 MeV positron-annihilation line, can then be linked to specific atmospheric sites and physical environments.

Despite the combination of observations from six spacecraft, our analysis of the X17 flare falls short of explaining the behavior of the positron annihilation line width. We have offered some ideas for theoretical work and encourage the development of better scenarios for particle effects in the solar atmosphere. Crucial to observational guidance and verification of flare scenarios, however, is that we obtain high-cadence, high-resolution (E)UV spectroscopic

observations. TRACE images reveal details in the flare down to its angular resolution of 1 arcec and temporal resolution of a few seconds, suggesting that future observations should be obtained at even better resolution. Such observations should extend from the low chromosphere into the high-temperature corona to cover the entire range of coupled processes from particle acceleration and impact to atmospheric response and radiative cooling. The future Solar-B EUV Imaging Spectrometer (EIS; e.g., Culhane *et al.*, 2005) fulfills some of these requirements by providing spectral coverage for transition-region and coronal temperatures with 2 arcsec angular resolution and a temporal resolution of a second or less for the brightest events. The high-temperature channels of the Atmospheric Imaging Assembly of the Solar Dynamics Observatory will enable us to image the rapid evolution of the coronal plasma. Comprehensive coverage from chromosphere to corona, however, will require even more powerful future instrumentation.

We thank the referee for guiding us towards a clearer presentation of the various aspects of the flare in comparison to the standard flare scenario. This work was supported by NASA under the TRACE contract NAS5-38099 with NASA Goddard Space Flight Center and MDI-SOI contract NAS5-30386 with NASA through Stanford contract PR 9162 (CJS, TDT), the RHESSI contract NAS5-98033 with NASA Goddard Space Flight Center(HSH), and NASA grants DPR-NNG05HL38l and DPR-NNG04ED18l (RJM, GHS).

REFERENCES

Allred, J. C., Hawley, S. L., Abbett, W. P. & Carlsson, M. 2005, ApJ 630, 573

Culhane, J. L., Harra, L. K., Doschek, G. A, Mariska, J. T., Watanabe, T. & Hara, H. 2005 Adv. in Space Res. 36, 1494

Ding, M. D., Qiu, J., & Wang, H. 2002, ApJL 576, 83

Donea, A.-C. & Lindsey, C. 2004, in *ESA SP-559: SOHO 14 Helio- and Asteroseismology: Towards a Golden Future*, p. 152

Emslie, A. G., Dennis, B. R., Holman, G. D., & Hudson, H. S. 2005, JGR 110, 11103

Fletcher, L., Pollock, J. A., & Potts, H. E. 2005, SPh 222, 279

Gros, M., Tatischeff, V., Kiener, J., Cordier, B., Chapuis, C., Weidenspointner, G., Veddrenne, G., Kienlin, A., Diehl, R., Bykov, A., & Méndez, M. 2005, in *5th INTEGRAL science workshop*, ESA SP552, ASP, Noordwijk, The Netherlands

Handy, B. N., Acton, L. W., Kankelborg, C. C., *et al.* 1999, SPh 187, 229

Hudson, H. S., Wolfson, C. J., & Metcalf, T. R.2006, SPh, 234, 79

Hurford, G. J., Schwartz, R. A., Krucker, S., Lin, R. P., Smith, D. M. & Vilmer, N. 2003, ApJL 595, 77

Hurford, G. J., Krücker, S., Lin, R. P., Schwartz, G. H., Share, G. H. & Smith, D. M. 2006, ApJL, submitted

Kozlovsky, B., Lingenfelter, R. E., & Ramaty, R. 1987, ApJ 316, 801

Kuznetsov, S. N., Kurt, V. G., Yushkov, B. Y., Myagkova, I. N., & Kudela, K. 2005, SPh, submitted

Lin, A. C., Nightingale, R. W., & Tarbell, T. D. 2001, SPh 198, 385

Lin, R. P., Dennis, B. R., & Benz, A. O. 2003, *The Reuven Ramaty High-Energy Solar Spectroscopic Imager (RHESSI)*, SPh 210, 1

Lin, R. P. & Hudson, H. S. 1976, SPh 50, 153

Machado, M. E., Avrett, E. H., Vernazza, J. E., & Noyes, R. W. 1980, ApJ 242, 336

Murphy, R. J., Dermer, C. D., & Ramaty, R. 1987, ApJSS 63, 721

Murphy, R. J., Kozlovsky, B., Share, G. H., Hua, X.-M. & Lingenfelter, R. E. , 2006 submitted to ApJ

Qiu, J. & Gary, D. E. 2003, ApJ 599, 615

Ramaty, R., Kozlovsky, B., & Lingenfelter, R. E. 1975, Space Sci. Rev. 18, 341

Ramaty, R., Mandzhavidze, N., Kozlovsky, B., & Murphy, R. J. 1995, ApJL 455, 193

Raymond, J. C., Cox, D. P., & Smith, B. W. 1976, ApJ 204, 290

Share, G. H., Murphy, R. J., Skibo, J. G., Smith, D. M., Hudson, H. S., Lin, R. P., Shih, A. Y., Dennis, B. R., Schwartz, R. A., & Kozlovsky, B. 2003, ApJL 595, 85

Share, G. H., Murphy, R. J., Smith, D. M., Schwartz, R. A., & Lin, R. P. 2004, ApJL 615, 169

Sudol, J. J. & Harvey, J. W. 2005, ApJ 635, 647

Vernazza, J. E., Avrett, E. H., & Loeser, R. 1981, ApJSS 45, 635

Warren, H. E., & Doschek, G. 2005, ApJL 618, 157

This preprint was prepared with the AAS LaTeX macros v5.2.

Table 1: Key events in the 2003/10/28 X17 flare.

Time (hh:mm:ss)	SOHO/MDI	TRACE	RHESSI, INTEGRAL, CORONAS
A 09:40:51		First signs of flare	*no RHESSI data until 11:06*
B 09:51:— X-ray flare start (GOES)			
C 11:02:30	first magnetogram artifact at P_1		first MeV continuum in INTEGRAL and CORONAS
D 11:04±4	peak acoustic power at P_1		
E 11:04:30	end magnetogram artifacts at P_1		peak in $26-100$ MeV in CORONAS
F 11:06:21		extremely bright 1600Å features ($> 4,000\times$ quiescent plage).	peak in 2.22 MeV in INTEGRAL; start of weakening of all γ rays in CORONAS and INTEGRAL
Share *et al.* (2004) 0.511 MeV line phase *a* 11:06:20-11:08:20: $\log T \sim 5.6$; $\log n \gtrsim 11$			
G 11:06:30	magn. polarity artifact at P_3		
H 11:06:46			RHESSI out of eclipse: 2.2 MeV line brightest in thick white circles, 100-200 keV bremsstrahlung in thin circles in Fig. 2d.
I 11:07±4	peak acoustic power at P_3		
J 11:07:41		very bright site (with diffraction cross) in 195Å (green dot in Fig. 2d; $> 7,500\times$ quiescent plage).	
Share *et al.* (2004) 0.511 MeV line phase *b* 11:08:20-11:10:20: $\log T \sim 5.3$; $\log n \gtrsim 13.5$			
K 11:09:30		1600Å impact site reaches umbra	
L 11:10:— $1-8$ Å X-ray flare peak (GOES)			
Share *et al.* (2004) 0.511 MeV line phase *c* 11:10:20-11:16:20: $\log T \sim 5.6$; $\log n \gtrsim 14.5$			
M 11:10:30	magnetogram polarity artifact at P_2		
N 11:11:30	magnetogram artifacts at red dot in Fig. 2d.		
O 11:16:30	magnetogram polarity artifact disappears at P_3; magnetogram artifacts continue to fade		0.511 MeV line narrowing from $\sim$7 keV to $1-2$ keV
Share *et al.* (2004) 0.511 MeV line phase *d* 11:16:20-11:18:20: $\log T \sim 5.0$; $\log n \gtrsim 15$			
Share *et al.* (2004) 0.511 MeV line phase *e* 11:18:20-11:30:20: $\log T \sim 3.8$; $\log n \gtrsim 15$			
P 11:19:30	magnetogram artifact at P_3 disappears		0.511 MeV line at 1-2 keV
Q 11:20:30	last signature of magnetogram artifacts at P_2		
R 11:30			end analysis by Share et al.

Fig. 1.— Flare lightcurves: *(a)* bremsstrahlung flux at 200 keV (pluses), nuclear de-excitation line flux (crosses; scaled by 0.1), and 0.511 MeV flux (triangles; scaled by 0.1; data from Share et al., 2004). The densely-clustered plus symbols up to 11:10:30 UT show the INTEGRAL ACS data scaled (by a factor 0.012) to the RHESSI 200 keV fluxes from 11:06 UT onward. Letters along the horizontal axis identify key events and features as listed in Table 1. The smooth solid curve is given by $16\,\exp(-t/3.6)+\exp(-t/20.)$ and the dotted straight line by $75\,\exp(-t/3.6)$ with t in minutes; *(b)* 0.511 MeV line width (from Share et al., 2004); *(c)* average intensity for the TRACE 1600 Å channel for the field of view as in Fig. 2, after subtraction of an average pre-flare level of 140 DN/s and a standard readout pedestal of 87 DN; symbol size increases with decreasing exposure duration. Thick curve: scaled 0.511 MeV line flux from panel *(b)* for comparison. The dashed-dotted line in the GOES $0.5-4$ Å signal (saturated around the flare peak, scaled by 10^6). The dotted line is $10^4\,\exp(-t/3.6)$,the dashed line $625\,\exp(-t/20.)$, and the thin solid curve is their sum; *(d)* TRACE 195 Å average intensity for the entire fov, after subtraction of a pre-flare level of 2 DN/s and a standard readout pedestal of 87 DN; symbol size increases with decreasing exposure duration. The dashed-dotted line is the GOES $0.5-4$ Å signal multiplied by 10^5, while the solid curve shows the GOES $1-8$ Å signal multiplied by $2.5\,10^4$. The long-dashed line is $85\,\exp -t/20$; *(e)* The histogram shows the total area of MDI magnetogram artifacts (in pixels). Also shown are the summed INTEGRAL γ-ray fluxes in the 4.4 MeV (C) and 6.1 MeV (O) lines (diamonds) until 11:06 UT, multiplied by 240, and the RHESSI nuclear de-excitation fluxes shown after 11:06 UT multiplied by 40.

Fig. 2.— *(a)* TRACE 'white light' image of the main spot cluster in AR 10486, observed on 2003/10/28 at 10:51:31 UT The green and red contours outline the penumbral and umbral boundaries, respectively. The solid-white and dashed-white contours outline the areas of strong negative and positive polarities, respectively (compare panel *(b)*). Overlaid as colored pixels are the magnetogram artifacts; the color coding (shown on the side bar) has time increasing uniformly from 11:01 UT to 11:18 UT. *(b)* MDI magnetogram taken at 11:11 UT. *(c)* Negative, logarithmically-scaled 1600 Å TRACE image taken at 11:11:44 UT. *(d)* Negative, logarithmically-scaled 1600 Å TRACE image taken at 11:17:01 UT. Also shown (and labeled by the time, showing mm:ss after 11 UT, are: thin bars, the locations of the very bright 1600 Å features causing CCD blooming at 11:06 UT, with one somewhat ambiguous one shown dotted; thick white circles: brightest sources for the 2.2 MeV line at 11:06 UT; thin white circles: brightest sources for the $100-200$ keV emission at 11:06 UT; green dot: the brightest point in the 195 Å image at 11:07:41 UT; red dot: artifact in the MDI magnetogram at 11:11 UT. The contours in panel *(a)* are repeated in each panel.

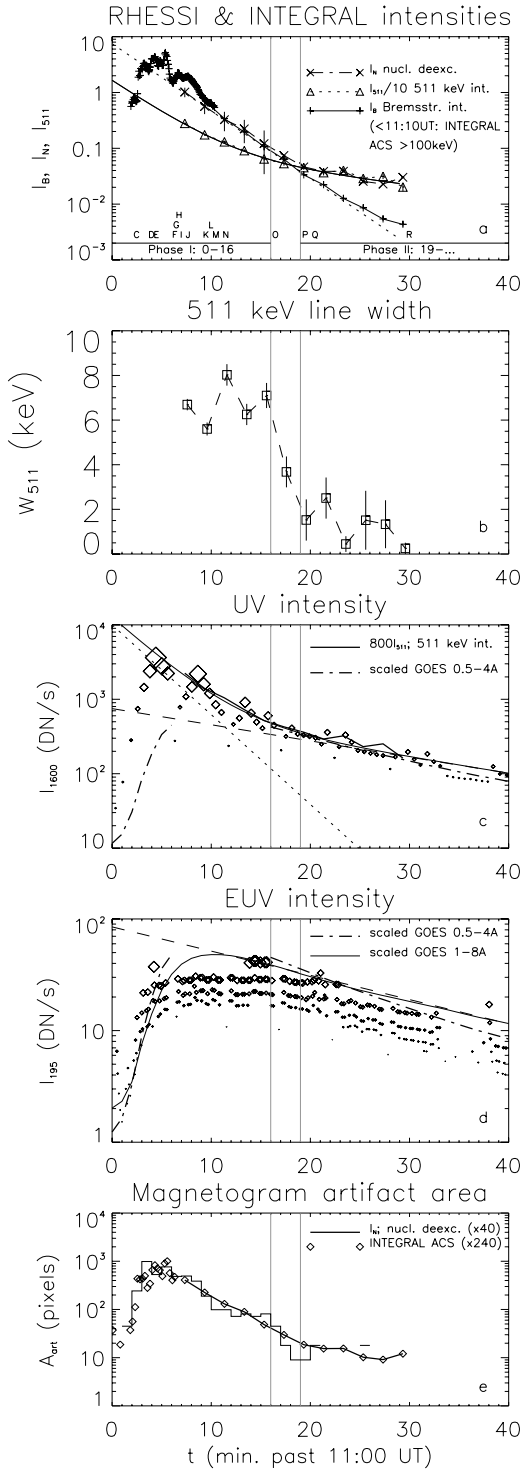

f1.ps

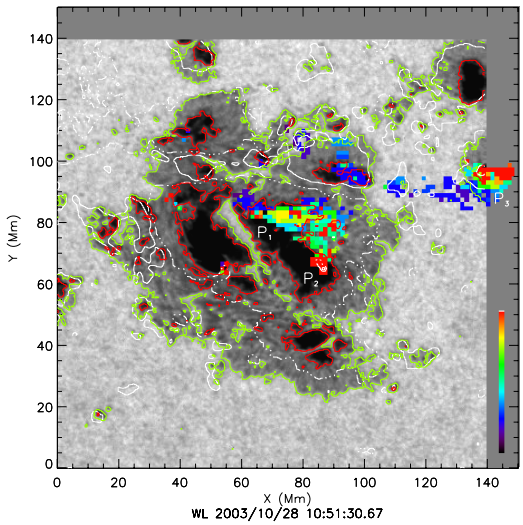

f2a.ps

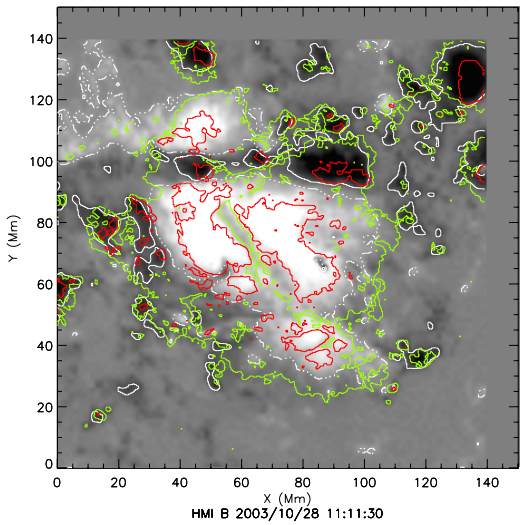

f2b.ps

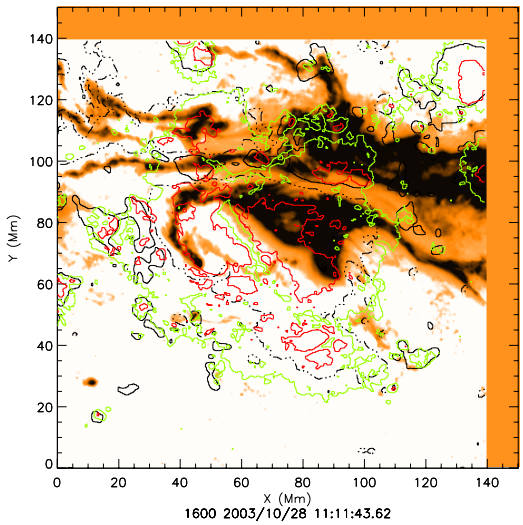

f2c.ps

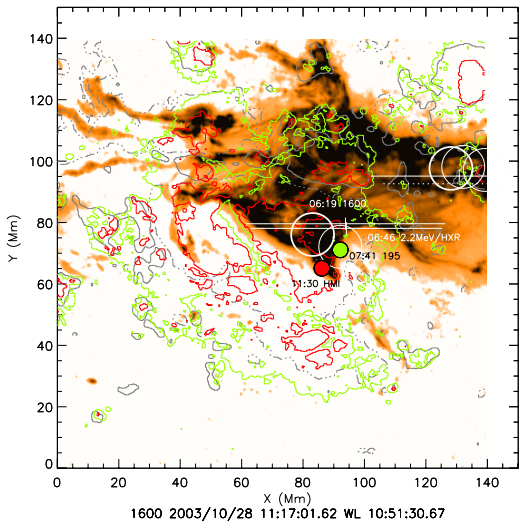

f2d.ps